Alma Mater Studiorum Università di Bologna
Archivio istituzionale della ricerca

Radio Science Investigations with the Asteroid Impact Mission

This version is available at: https://hdl.handle.net/11585/651429 since: 2019-09-27

Published:

DOI: http://doi.org/10.1016/j.asr.2017.12.003

(Article begins on next page)

Radio Science Investigations with the Asteroid Impact Mission

Marco Zannoni[1*] (m.zannoni@unibo.it), Giacomo Tommei[2] (giacomo.tommei@unipi.it), Dario Modenini[1] (dario.modenini@unibo.it), Paolo Tortora[1] (paolo.tortora@unibo.it), Ruaraidh Mackenzie[3] (ruaraidh.mackenzie@esa.int), Mehdi Scoubeau[3] (mehdi.scoubeau@esa.int), Ulrich Herfort[3] (ulrich.herfort@esa.int), Ian Carnelli[4] (ian.carnelli@esa.int)

[1]Department of Industrial Engineering, University of Bologna, Via Fontanelle 40, I-47121 Forlì, Italy

[2]Department of Mathematics, University of Pisa, Largo Bruno Pontecorvo 5, I-56127 Pisa, Italy

[3]ESA/ESOC, Robert-Bosch-Strasse 5, D-64293 Darmstadt, Germany

[4]ESA/HQ, 8-10 Rue Mario Nikis, F-75738 Paris, France

[*]Corresponding author

Abstract

The Asteroid Impact & Deflection Assessment (AIDA) mission is a joint ESA/NASA collaboration to study the binary Near-Earth Asteroid (65803) Didymos and assess the feasibility of the kinetic impactor technique to deflect an asteroid. The European contribution to AIDA is the Asteroid Impact Mission (AIM), which will characterize in detail the Didymos system, investigating the surface, subsurface, and internal properties of the asteroid.

This paper presents a possible Radio Science Experiment (RSE) to be performed with AIM focused at its precise orbit determination within the Didymos system, providing an assessment of the accuracies achievable in the estimation of the scientific parameters of interest, like the masses and the extended gravity fields of Didymos primary and secondary, their relative orbit, and their rotational states. The experiment expected performances were assessed through numerical simulations, based upon a complete and realistic dynamical model of the Didymos system and the AIM spacecraft.

Given the small mass of the Didymos system, optical navigation images proved to be crucial to obtain good accuracies for the scientific parameters of interest, even keeping AIM at relatively large distances from Didymos. At 10 km, after 8 flybys dedicated to gravity science, the masses of the primary and secondary can be estimated to about 0.2% and 1.6% (1-sigma), respectively, with the mass of the secondary being mainly given by observing the wobble of the primary around the common center of mass due to the mutual orbital motion; the orbital motion of the secondary around the primary can be estimated to about 1 m, and the pole orientation of the primary and the secondary can be estimated to about 0.1 deg and 0.4 deg, respectively (1-sigma).

Keywords: Orbit determination; Near-Earth asteroids; Binary asteroids.

1. Introduction

The study of multiple asteroid systems is a relatively young field of research, but very important because such objects enable investigations of properties and processes that are difficult to verify by other means (see Margot et al. 2015 for a brief review of asteroid systems). The existence of binary asteroids was disputed until 1993, when Galileo spacecraft, during a fly-by, discovered the satellite Dactyl of (243) Ida. A few years later, due to the increase of ground-based efforts, a satellite around (45) Eugenia was discovered.

Since then, many binary asteroids have been found using different observation techniques and now binaries are known to exist among almost all dynamical classes of minor planets: NEAs binaries are a significant fraction, about 15±4%, of the entire population (Pravec et al., 2006).

The Asteroid Impact Mission (AIM) is a candidate ESA mission to the binary Near-Earth Asteroid (65803) Didymos (Michel et al., 2016). AIM would characterize for the first time a binary asteroid system, providing an understanding of its formation and evolution, and of the origin of the entire Solar System. AIM can be conceived as a stand-alone mission, but it is also the ESA contribution to the proposed joint mission AIDA (Asteroid Impact & Deflection Assessment), which includes also NASA's spacecraft DART (Double Asteroid Redirection Test) (Cheng et al., 2015)(Cheng et al., 2016). DART would impact the secondary of Didymos to test and validate the kinetic impactor as a planetary protection strategy and greatly increase the scientific return of both missions through the detailed comparison of the Didymos system before and after the impact. In addition to its own scientific payload, AIM is planned to carry some smaller probes (Mascot-2 asteroid lander, developed by DLR, and two or more CubeSat Opportunity Payloads (COPINS)).

A binary asteroid system is an intrinsically complex dynamical environment, characterized by a strong coupling between the rotational and orbital dynamics of the two bodies. Measuring their orbital and rotational dynamics could be useful to possibly characterize the main effects on the long-term behavior of the binary, like the spin-orbit resonance, the Yarkovsky-O'Keefe-Radzievskii-Paddack (YORP) effect and the Binary YORP (BYORP) effect.

Besides the scientific relevance, an accurate estimation of the orbit and the gravity of the secondary is very important also for the AIM mission operations, to ensure a safe navigation in the proximity of the system, as during the deployment of the smaller probes.

Moreover, in the context of the AIDA mission, the precise characterization of the Didymos system provided by AIM could greatly enhance the study of the effects of the DART impact on the secondary, through comparisons between the system properties before and after the impact.

This paper describes a possible Radio Science Experiment (RSE) in the framework of the AIM mission: exploiting the radiometric measurements, acquired between the spacecraft and the Earth, and optical measurements of Didymos taken by the spacecraft, it is possible to perform a precise orbit determination of the probe within the Didymos system, estimating, at the same time, a number of dynamical parameters of scientific interest. First, reconstructing the relative orbits of AIM, Didymos primary, and secondary, an estimation of the masses of Didymos can be obtained, which can then be used together with their shapes to derive the bulk densities and their average composition. Then, the degree-2 gravity coefficients of the bodies provide information about their internal mass distribution, while higher degree coefficients may highlight the presence of local density anomalies through a gravity-topography comparison. A realization of the body-fixed frames of the bodies is obtained estimating the coordinates of a number of surface topographic feature, known as landmarks. Finally, measuring the time evolution of the frames, along with the gravities, provides additional information about the moments of inertia of the bodies, and their internal mass distributions.

Numerical simulations were carried out during this study, with the following goals: assess the feasibility of performing Radio Science investigations of the Didymos system with the AIM mission; provide a preliminary evaluation of the accuracies achievable in the estimation of the scientific parameters of interest; provide guidelines to maximize the scientific return of the entire mission.

The paper is organized as follows: Section 2 describes the baseline AIM mission scenario used as an input for the study; the procedure adopted for the numerical simulations is outlined in Section 3; Section 4, Section 5, and Section 6 describe in detail the dynamical model implemented in the simulations, the generation of simulated measurements, and the setup of the estimation filter, respectively. The main results of the simulations are provided and discussed in Section 7. Finally, Section 8 summarizes the main findings and conclusions of this work.

2. AIM Mission Scenario

To assess the orbit determination performances, the mission scenario must specify: the relative geometry between the Sun, the Earth, and the Didymos system that, given the orbits and rotational models of the celestial bodies, is provided by the mission timeline; the relative geometry between the spacecraft and the Didymos system during the radio science experiments, which is usually driven by the mission objectives and operational constraints.

The AIM mission timeline adopted during this study is represented in Table 1: the launch is scheduled in October-November 2020, while the arrival to Didymos system is in May 2022. Radio science investigations will be carried out mainly before CubeSats and Lander deployment. Hence, the main dynamical properties of the system shall be characterized with a sufficient accuracy during the Early Characterization Phase (ECP), Detailed Characterization Phase 1 (DCP1), and Payload Deployment Phase (PDP), to ensure a safe navigation in proximity of the Didymos system during these critical events. The observations after the lander deployment, during the Detailed Characterization Phase 2 (DCP2), and after the Impact Phase, during the Detailed Characterization Phase 3 (DCP3), will be used respectively to improve the estimation accuracy and to estimate the changes in the dynamical model of the Didymos binary system due to the DART impact. During the adopted mission timeline the Sun-Earth-Probe (SEP) angle is always larger than 90 deg, resulting in favorable conditions for spacecraft operations, in terms of achievable telemetry data rate and radiometric noise levels. The results of this study are expected to be representative also for different mission timelines, with small quantitative variations because several conservative assumptions were made during the study, absorbing possible changes in the relative Sun-Earth-Didymos geometry.

Regarding the Didymos-AIM relative geometry, a mission concept similar to Rosetta was assumed: the AIM reference orbit consists of a series of hyperbolic arcs connected by impulsive maneuvers to form pyramid-like trajectories. This strategy is much more flexible and offers several operational advantages (Herfort and Casas, 2015): lower sensitivity to errors in gravity potential; lower sensitivity to errors in the maneuvers; more favorable illumination conditions, both for science observations and optical navigation; safe escape trajectory in case of spacecraft problems.

The same strategy was adopted for the radio science investigations, which should be performed during a limited number of hyperbolic arcs connected to the pyramid-like reference trajectory. Table 2 provides the parameters which completely defines the Didymos-AIM relative hyperbolic trajectory, and the corresponding range of values assumed during this study.

The results reported in this paper were obtained assuming 8 non-contiguous flybys dedicated to the Radio Science Experiment. To make comparisons between different strategies, all the 8 flybys were designed to have the same configuration (spacecraft initial conditions, arc length, noise levels, …), except for the relative position between the spacecraft and Didymos secondary at the time of flyby pericenter. Being the flyby geometry fixed, this relative position is completely defined by the true anomaly of Didymos secondary along its orbital motion around the primary. In order to reduce the number of simulations and better de-

correlate the gravity fields of Didymos primary and secondary, the timing of each radio science flyby was chosen to have a different true anomaly of Didymos secondary at the pericenter epoch, uniformly distributed between 0 and 360 deg. An example of the spacecraft trajectories during the radio science flybys is represented in Figure 2. Then, a series of simulations were performed to assess the sensitivity of the experiment performances to different orbital geometries. For each mission phase studied, characterized by a different distance from the system, the flyby plane was chosen to minimize the uncertainties in the GM of Didymos primary and secondary, which are the main scientific parameters of interest. The real AIM Radio Science Experiment may employ a combination of a different number of flybys, each with a different geometry, for example to gradually reduce the distance to Didymos for safety reasons.

3. Simulation Procedure

A gravity radio science experiment represents a particular application of the orbit determination process, whose aim is to estimate a set of parameters to completely define the past trajectory of the spacecraft and predict its future evolution. To assess the formal accuracies of the estimated parameters before the execution of the experiment, numerical simulations may be implemented, performing the same orbit determination procedure for the analysis of real data, but using simulated data. Moreover, controlling the dynamical model used to generate the simulated measurements, it is possible to provide a better understanding of the effects of the main design parameters which affect the performances of the experiment.

In this work the same models are used to compute the simulated observed and computed measurements, performing a so-called "covariance analysis". The output of a covariance analysis is useful to compare different solutions, obtained for example using different orbital geometries, coverage assumptions, filter setups. However, the real uncertainties associated to estimated parameters are usually larger than the formal values provided by the orbit determination, because the classical procedure does not consider possible estimation biases due to errors in the dynamical model, linearization errors, colored measurement noise, and other effects. For this reason, in the numerical simulations of the AIM Radio Science Experiment a series of conservative assumptions were made to obtain more realistic estimation uncertainties, namely: the adopted Doppler measurement noise is larger than the expected level by more than a factor of 2; the adopted optical measurement noise is larger than the expected level by a factor of 2-20; large a priori uncertainties on the solve-for parameters were used.

The numerical simulations were performed using JPL's orbit determination program MONTE (Mission Analysis, Operations, and Navigation Toolkit Environment), currently used for the operations of all NASA's space missions managed by JPL (Evans et al., 2016) and for radio science data analysis (see e.g. (Iess et al., 2014) and (Tortora et al., 2016)). MONTE's mathematical formulation is described in detail in (Moyer, 1971) and (Moyer, 2000).

4. Dynamical Model

As a part of the orbit determination process of the AIM spacecraft, all the relevant dynamics must be modeled and updated, namely: the orbit of the Didymos system within the Solar System, the relative orbit between Didymos secondary and primary, and the relative orbit of the spacecraft with respect to the Didymos system.

To better understand the dynamical environment within the Didymos system and to build a realistic dynamical model, the order-of-magnitude of the main gravitational and non-gravitational accelerations acting on a spacecraft were computed for different distances from Didymos. The resulting values are collected in Table 3. As a result, the orbits of Didymos secondary and AIM were computed numerically integrating the equations of motion with respect to the system center of mass, using the following gravitational accelerations: point-mass accelerations due to the Sun, all the planets of the Solar System, the Moon, and Pluto; point-mass accelerations due to Didymos primary and secondary, along with the accelerations due to their gravity spherical harmonics.

The dynamical model also included the main non-gravitational accelerations acting on the spacecraft: the Solar Radiation Pressure (SRP), using a realistic shape model of AIM, and the Thermal Recoil Pressure (TRP). The total SRP on the spacecraft is computed as the sum of the forces acting on its components, each with different geometry, surface properties, and orientation with respect to the Sun. The components used to model the spacecraft shape, along with their properties, are summarized in Table 4. The TRP arises from an anisotropic emission of the thermal flux radiated into space to keep a thermal equilibrium condition. The TRP acting on the spacecraft is function of its shape, orientation with respect to the Sun and other celestial bodies, its surface properties, and its thermal state. For simplicity the TRP is modeled as a constant acceleration in the body-fixed frame, with a nominal zero value. As a reference, using precise analytical models of the Rosetta spacecraft, the TRP was estimated to be 5-10% of the SRP (Kato and van der Ha, 2012). One of the main source of error in the orbit determination are the modelization errors of the non-gravitational accelerations. In order to take into accounts these effects, a scale factor for the SRP and the three Cartesian components of the TRP were estimated as a part of the orbit determination process.

The following accelerations were not used in the integration, because considered to be negligible: the relativistic perturbative accelerations due to all bodies but the Sun; the acceleration on Didymos secondary due to its own spherical harmonics (indirect oblateness); the non-gravitational accelerations on Didymos secondary due to Solar Radiation Pressure, albedo and thermal emissions, because of its low area-to-mass ratio; the non-gravitational accelerations on AIM due to primary and secondary albedo and thermal emissions.

The initial conditions of Didymos secondary were computed assuming an equatorial, circular orbit with respect to the primary, with a semi-major axis of 1.18 km (Scheirich and Pravec, 2009)(Fang and Margot, 2012). The distance between Didymos primary and the system center of mass is about 11 m.

The rotational models of Didymos primary and secondary influence the gravitational accelerations acting on Didymos secondary and on the spacecraft. The pole orientation of Didymos primary and secondary with respect to the Earth Mean Orbit at J2000 (EMO2000) is described by its right ascension α and declination δ, modeled as linear functions of time:

$$\alpha = \alpha_0 + \alpha_1(t - t_0) \tag{1}$$
$$\delta = \delta_0 + \delta_1(t - t_0) \tag{2}$$

The orientation of prime meridian of Didymos primary with respect to the node is described by the angle w, modeled as a linear function of time, corresponding to a uniform rotation:

$$w = w_0 + w_1(t - t_0) \tag{3}$$

In addition to a uniform rotation, the prime meridian of Didymos secondary may experience a libration with angular velocity ω, amplitude w_a, and phase φ:

$$w = w_0 + w_1(t - t_0) + w_a \sin[\omega(t - t_0) + \varphi] \tag{4}$$

The Didymos primary rotational model was adopted from (Scheirich and Pravec, 2009) and (Osip et al., 2016), while the rotational model of the secondary was built assuming a synchronous rotation around the primary, with the addition of a libration at the orbital period of amplitude 1 deg, consistent with the value reported in (Richardson et al., 2016). The corresponding numerical values defining the rotational models are collected in Table 5. A drift of less than 30 deg/century in the pole orientation of the secondary was obtained; the drift is caused by the perturbations on the relative orbit of the two bodies, caused by the Sun (mainly) and the Earth.

All the coefficients of the rotational models of Didymos primary and secondary were estimated during the simulations.

The gravitational masses (GM) of Didymos primary and secondary were computed from their diameter ratio and the total mass of the system (Fang and Margot, 2012), assuming the same density. The resulting primary and secondary GM are 3.4903x10^{-8} km^3/s^2 and 3.23x10^{-10} km^3/s^2, respectively, with a mass ratio of about 0.01.

Didymos primary extended gravity is modeled using a spherical harmonics expansion up to degree 20, whose coefficients were obtained from the polyhedral shape. Several methods are available in literature to compute the gravity spherical harmonics expansion of a homogeneous polyhedron (Werner, 1997)(Tsoulis et al., 2009). However, for simplicity, the following procedure was used: the input polyhedron was represented as a spherical harmonic expansion of degree 20 through a least squares fit of the vertices of the polyhedron. The degree was chosen to obtain a resolution comparable to the polyhedral representation. Then, the shape coefficients of the series were converted to gravity coefficients, under the assumption of uniform density, following (Wieczorek, 1998). As reference, the resulting normalized degree-2 gravity coefficients of Didymos primary are collected in Table 6. The corresponding gravity field coefficients are represented in Figure 1.

Didymos secondary extended gravity is modeled using the degree-2 spherical harmonics expansion of a homogeneous tri-axial ellipsoid, aligned with the body-fixed axes, with semi-principal axes a = 103 m, b = 79 m, c = 66 m (Pravec et al., 2006)(Richardson et al., 2016). The degree-2 normalized gravity coefficients are provided in Table 6; the only non-zero terms were computed using the following equations (Bills et al., 2014):

$$\bar{C}_{20} = \frac{1}{\sqrt{5}} \frac{2c^2 - (a^2 + b^2)}{10a^2} \tag{5}$$

$$\bar{C}_{22} = \sqrt{\frac{12}{5}} \frac{a^2 - b^2}{20a^2} \tag{6}$$

The gravitational parameters and the degree-2 coefficients of Didymos primary and secondary were estimated as a part of the orbit determination process.

5. Measurement Models

Each radio science arc starts at C/A − 36 h and ends at C/A + 36 h, where C/A is the time of closest approach to the Didymos system center of mass. An orbital maneuver is executed just before the arc start and just after the arc end, to connect the arc, optimized for radio science investigations, to the pyramid-like reference trajectory. The flyby timeline is represented in Figure 3.

During the arc both two-way Doppler and optical navigation observables are collected: given the typical small relative velocities and accelerations near Didymos system, the classical Doppler measurements, usually adopted as main observable in the interplanetary orbit determination process, provide a limited information content. Hence, the spacecraft navigation must be enhanced by means of additional observations, like optical measurements obtained by the onboard cameras. When aiming at a distant target, the picture of a body provides its relative direction with respect to the spacecraft, in the camera frame (centroid). When near, the camera may be used to identify optical features on the surface of a body (landmarks), allowing to better estimate also its rotational state. Additionally, in a binary system the optical measurements provide also the accurate relative positions of the two bodies, posing a strong constraint on their relative orbital motion. The relative orbital motion provides information about the total mass of the system but, if the mutual orbital motion is measured with respect to the common center of mass, which is inertially fixed, also the mass ratio can be obtained. The inertial motion of the secondary provides information mainly about the mass of the primary, and vice versa.

However, the optical measurements are affected by a scaling symmetry, because they do not provide direct information about the relative distance with respect to a body: the same optical measurements can be obtained changing the distance AIM-body and the size of the body by the same scale factor S. The scaling symmetry affects also the estimation of the body mass: in the approximation of the two-body problem, during the orbital motion the same series of pictures can be obtained changing the body mass by S^3. The scaling symmetry applies also to a binary system: the same optical measurements can be obtained changing also the distance primary-secondary by the same scale factor. The scaling symmetry can be constrained using a priori information about the estimated parameters, and different observables, like Doppler and range, which provide absolute measurements of velocity and distances with respect to the Earth.

The nominal Doppler coverage assumed in the simulations consists of three 8 h tracking passes centered around the start maneuver and the end maneuver, to aid the spacecraft navigation, and around the pericenter, to improve the sensitivity to the gravity fields (Figure 3). The arc starts just after the start maneuver, and ends just before the end maneuver, so that only 4h of data during the first and last tracking passes were used in the estimation, for a total coverage of 16 h. During scheduled tracking passes two-way Doppler measurements between AIM and an Earth ground stations are simulated, with a count time of 60 s, and then degraded adding a white Gaussian noise. During the filtering procedure, Doppler data are weighted using directly the input noise level. The noise level expected on Doppler observables was computed using simplified models of the main noise sources (Iess et al., 2014). Then, for simplicity, a constant noise level of 0.051 mm/s at 60 s integration time was adopted as a nominal value, corresponding to the maximum expected noise during the AIM mission, multiplied by a conservative factor of 2. As a comparison, the two-way X/X Doppler measurements of the Dawn spacecraft were characterized by a noise of about 0.02 mm/s at 60 s integration time (Konopliv et al., 2014), while the X/X Doppler measurements of the Rosetta spacecraft were characterized by a noise of about 0.090 mm/s, scaled to 60 s integration time (Godard et al., 2015).

Between tracking periods, when the spacecraft does not have to point the fixed HGA to the Earth, optical observables are acquired, with a nominal sampling time of 2 h (Figure 3). At each sampling epoch one picture of Didymos primary and one picture of Didymos secondary are taken. For operational constraints of the AIM spacecraft, a picture of Didymos can be acquired only if the angle Sun-Didymos-AIM, also called Sun phase angle, is less than 60 deg. The optical observables used in the orbit determination are the line and pixel location of all the surface landmarks visible in the image. If the body size on the picture is smaller

than 100 pixels, the centroid is used as observable instead of the landmarks. The same characteristics of the navigation camera of Rosetta were used to generate the simulated optical observables (Pardo de Santayana and Lauer, 2015). The line and pixel coordinates of the landmarks (or centroids) are degraded adding a white Gaussian noise with a constant standard deviation of 2 pixel. This value is about two times the accuracy in the optical measurements of Rosetta (Godard et al., 2015) and 20 times the corresponding accuracy of Dawn (Konopliv et al., 2014). A total of 528 landmarks were generated on the surface of Didymos primary and secondary, uniformly spaced in latitude and longitude by 15 degrees. As reference, for Rosetta orbit determination the number of landmarks was between 50 (during high altitude orbits) and 1000 (low altitude orbits) (Pardo de Santayana and Lauer, 2015). A picture provides an angular measurement of a body relative to the spacecraft, in the frame of reference of the camera. The relative direction is translated in the inertial frame knowing the spacecraft attitude and the body-fixed camera orientation. However, an error in the inertial pointing of the camera propagates directly to the relative position of the spacecraft with respect to the body. For this reason, a pointing correction is estimated for each picture, as in (Konopliv et al., 2014). The pointing error is modeled as three rotations, with a priori 1-sigma uncertainty of 10 mdeg. This is the same value used in the orbit determination analysis of Rosetta (Godard et al., 2015), but it is more than a factor 2 larger than the values used for Dawn (Konopliv et al., 2014). Conservative values of pixel noise and pointing errors were adopted to approximately account for errors in the optical measurements difficult to model, like landmark misdetection or offsets between the body centroid and its center of mass.

Full Doppler coverage (without optical measurements) and full optical coverage (without Doppler) were also analyzed, for comparison purposes only: in fact, both optical and radiometric measurements are usually essential for a safe spacecraft navigation around small bodies, because their combination allows a more reliable and robust orbit determination and to estimate additional mission-critical parameters, like the orbital maneuvers and the heliocentric trajectory of the Didymos system. To better understand the information content carried by the optical measurements, cases with pictures of only one body (either the primary or the secondary) were also analyzed.

6. Filter Setup

The multi-arc approach will be adopted for the radio science investigations of the AIM mission: the data obtained during non-contiguous orbital segments, called "arcs", are combined and jointly analyzed in a weighted least-squares filter to produce a single solution of a set of solve-for parameters. As a consequence, the scientific results will be obtained at the end of the mission, by post-processing of all available arcs, as opposed to the output of the operational orbit determination, which must be as much as possible in "real time", to safely navigate the spacecraft. The solution is formed by the estimated values of the parameters and the corresponding covariance matrix, which provides the formal estimation uncertainties. The multi-arc strategy is commonly used in the data analysis of radio science experiment (Iess et al., 2012)(Iess et al., 2014)(Modenini and Tortora, 2014)(Tortora et al., 2016).

The solve-for parameters can be classified into two groups: global parameters, which do not vary with time and affect the measurements of all the arcs (e.g. the gravity fields), and local parameters, which affect only the measurements of a single arc (e.g. the arc initial conditions of the spacecraft). However, parameters which in principle are global may be treated as local, to absorb modelization errors. For example, in this work the SRP scale factor is estimated as a local parameter, to take into account possible variations of the reflectivity properties of the spacecraft surfaces during the mission. Note that this approach is conservative, as the parameters uncertainties would increase because of the correlations. Moreover, also

the orbit of the secondary was estimated locally on each arc: in the adopted mission scenario, the radio science flybys may be separated by long periods of time, much larger than the mutual orbital period. In this situation, a "small" error in the initial conditions, in the order of the estimation uncertainty, may accumulate over time, leading to a significantly different orbital position at the end of the mission. The filter setup adopted in the study is summarized in Table 7, where it is specified if each parameter, or group of parameters, is treated as local or global, and the corresponding a priori 1-sigma uncertainty.

7. Results

At first, a series of simulations were performed to assess the RSE performances achievable during the three phases of the AIM mission before the deployment of the CubeSats and the Lander, each characterized by a different distance from the Didymos system:

- Early Characterization Phase (ECP): the pericenter radius is 35 km, so this case provides a reference solution for long distances operations. Being outside the sphere of influence of Didymos for the entire duration of each arc, the Doppler observables are expected to provide very low information content about the gravity fields of the bodies.
- Detailed Characterization Phase 1 (DCP1): the pericenter radius is 10 km, so being near the boundary of the sphere of influence of Didymos the Doppler observables are expected to provide some information content about the gravity fields of the bodies.
- Payload Deployment Phase (PDP): the pericenter radius is 2 km, so this case provides a reference solution for very short distances operations. Being inside the sphere of influence of Didymos the Doppler observables are expected to provide a large information content about the gravity fields of the bodies.

A summary of the formal 1-sigma uncertainties achievable in the estimation of the main parameters of interest during these phases is provided in Table 8. Both Doppler and optical measurements are processed, assuming the nominal coverage described in Section 5. For each phase, the orbital geometry is chosen as a best compromise to minimize the uncertainty in the GM of Didymos primary and secondary. Table 9 provides the 1-sigma uncertainties for a subset of the estimated parameters for the same cases, but processing pictures of only one body, either the primary or the secondary.

Then, a number of simulations were performed to assess the information content provided by Doppler and optical navigation images. Figure 4 and Figure 5 show the 1-sigma uncertainty in the GM of Didymos primary and secondary, respectively, as a function of the pericenter radius of AIM and for different measurement strategies. For each pericenter radius and measurement strategy, the orbital geometry is chosen to optimize the estimation of the GM of each body. However, the optimal geometry for Didymos primary and secondary may be different, so that it is not possible to minimize the uncertainty in the GM of both bodies: for this reason the values displayed in Figure 4 and Figure 5 are, in general, smaller than the ones reported in Table 8, which were obtained for a specific orbital plane. The following measurement strategies were compared:

- Doppler: only Doppler measurements are processed, acquired at the beginning and end of the arc, and around the pericenter, as described in Section 5.
- Doppler (full): only Doppler measurements are processed, assuming a continuous coverage during the entire arc.
- Optical: only optical measurements are processed, acquired during the entire arc duration. No Doppler measurements are collected, so the number of pictures is larger than Doppler+Optical strategy.

- Optical (phase): only optical measurements are processed, acquired during the entire arc duration, but only if the Sun phase angle is smaller than 60 deg. No Doppler measurements are collected, so the number of pictures is, in general, larger than Doppler+Optical (phase) strategy.
- Doppler+Optical: both Doppler and optical measurements are processed, assuming the base coverage described in Section 5.
- Doppler+Optical (phase): both Doppler and optical measurements are processed, assuming the base coverage described in Section 5. The optical measurements are acquired only if the Sun phase angle is smaller than 60 deg. This represents the nominal measurement strategy assumed in this study.

From the results provided in Table 8, Table 9, Figure 4, and Figure 5, a number of general considerations can be made.

The Didymos primary-AIM relative position can be estimated at a level of 1% or better (1-sigma). The position uncertainty is in general dominated by the radial component, because it is directly affected by the scaling symmetry of the optical measurements. In fact, a picture of a single body provides a direct information on the body-camera relative distance only knowing the size of the body. If a picture of two bodies is taken, the relative camera-bodies range can be directly reconstructed also from the relative distance between the two bodies. If the two bodies are imaged through two different pictures, there is an additional degradation due to the pointing errors. As a consequence of the scaling symmetry, the orbit of Didymos secondary relative to the primary can be estimated with approximately the same relative uncertainty of the Didymos primary-AIM position. As expected, if pictures of only Didymos primary are taken, the estimation of the secondary orbit degrades significantly, by up to a factor of 110. The binary orbital period can be estimated with a 1-sigma uncertainty of about 14 minutes at 35 km, during ECP, decreasing to 0.64 minutes at 2 km, during PDP. As a reference, the DART impact on the secondary is expected to change the period by about 4 minutes (Cheng et al., 2016).

The GM of Didymos primary can be estimated with a relative 1-sigma uncertainty of about 2% at 35 km, improving with smaller distances to about 0.01% at 2 km. The information about the GM of Didymos primary is provided by both Doppler and optical measurements. The Doppler shift provides a measurement of the bending of the trajectory of AIM due to the gravity of the Didymos system, while optical navigation images provide a measurement of the primary GM reconstructing the orbital motion of the secondary, but they are affected by the scaling symmetry. The best accuracies are obtained using both Doppler and optical navigation images, so that the formal uncertainty decreases by more than a factor of 10, with respect to Doppler only and optical only. The quadrupole of Didymos primary cannot be fully estimated, even during the PDP.

The GM of Didymos secondary can be estimated at a level of about 5% at 35 km, improving with smaller distances to about 1% at 2 km (both 1-sigma). The GM of Didymos secondary is estimated mainly from optical measurements of Didymos primary, i.e. observing the wobble of the body around the common center of mass due to the mutual orbital motion, as proposed by (Grieger and Kuppers, 2016). In fact, for every pericenter radius the best results are obtained using only optical measurements, because the number of pictures acquired during the arc is maximized. Moreover, for distances larger than 5 km the estimation degrades significantly, by a factor of 20, if only optical measurements of Didymos secondary are taken. As a comparison, processing only pictures of the primary the estimation uncertainty increases only by about 15%. On the other hand, for distances smaller than 5 km the uncertainty increases by only 50%, in both cases. This is because the gravitational effect of Didymos secondary on AIM becomes significant, and consequently the Doppler-only uncertainty starts decreasing, even if it remains higher than the Optical case by a factor of 2. For larger distances, the GM cannot be estimated using Doppler only. However, using both Doppler and optical measurements the GM estimation becomes more reliable and robust (e.g. to a Sun phase angle constraint), while its formal uncertainty increases by less than 10%. The quadrupole of Didymos secondary cannot be estimated.

Applying the Sun phase angle constraint to the optical measurements the uncertainty increases significantly only for shorter distances, because the number of pictures which can be processed decreases. For example, at 35 km it is possible to find a geometry which keeps the phase angle below the maximum allowed value for the entire arc duration, while at 2 km the constraint can be satisfied at most for half the arc duration, reducing the number of optical measurements by about a factor of 2.

During DCP1 the orientation of the pole of Didymos primary and secondary can be estimated at a level of about 0.1 deg and 0.4 deg (1-sigma), respectively; the libration amplitude, period and phase of Didymos secondary can be estimated at a level of 0.03 deg (which corresponds roughly to a surface displacement of about 0.05 m, at the equator), 9.7 s, and 6.7 deg, respectively (all 1-sigma). The pole drift of the secondary cannot be estimated with sufficient accuracy. It is interesting to note that the uncertainties in the rotational states increase with smaller distances: this is because they can be estimated only through optical measurements, whose number decreases with the distance because of the Sun phase angle constraint.

The single-arc estimations, obtained using only one flyby, were compared to each other and to the multi-arc estimation to study how the synchronization between AIM and Didymos secondary orbits affects the experiment performance (Table 10). As a result, the synchronization of the two orbits does not play a significant role in the estimation accuracy, especially if the optical observables are used: for example, the uncertainties in Didymos primary and secondary GMs change by less than a factor of 1.2 and 1.5, respectively. Moreover, when the estimation is driven by optical observables, as for the GM of the secondary, the ratio between the single-arc and multi-arc uncertainties is about $\sqrt{8} \approx 2.8$, i.e. the square root of the number of flybys. This is an indication that each flyby provides roughly the same information content and can be considered as an independent measurement. On the other side, if the information content provided by Doppler observables is not negligible, as for the GM of the primary, the multi-arc estimation can improve the single-arc uncertainty up to a factor of 8.

The orbital geometry proved to be a driving factor of the estimation accuracy, because it defines: the gravitational pull on the trajectory, measured by the Doppler observables; the number of pictures which may be acquired, due to the Sun phase angle constraint; the surface coverage of the landmarks visible in the pictures of the two bodies. In particular, by decreasing the pericenter radius we obtain smaller uncertainties, by up to a factor of 100. Then, at a given pericenter distance, changes to the orbital plane cause the uncertainties to change by a factor of 10-100. Given the criticality of the optical measurements, the flyby geometry should be selected to optimize the number of pictures and the landmark coverage.

8. Conclusions

The main result of this paper is that the proposed AIM gravity Radio Science Experiment at Didymos proved feasible. The expected performances were assessed through numerical simulations, based upon a complete and realistic dynamical model of the Didymos system, and taking into account all the most important accelerations acting on the AIM spacecraft and Didymos secondary. Conservative assumptions on the mission scenario and the technological capabilities of the space and ground segment were made. As a result, the formal uncertainties provided by this study are expected to be representative of the real accuracies achievable by the AIM Radio Science Experiment.

Shorter pericenter distances increase the attainable accuracy, but good results can already be obtained at large distances using optical navigation images. During the Early Characterization Phase of the mission, when the AIM-Didymos distances will be in the order of 35 km, the masses of Didymos primary and secondary can be estimated to about 2% and 5% (1-sigma), respectively, using 8 flybys dedicated to gravity science. Moving to 10 km, as expected during the Detailed Characterization Phase 1, the uncertainties decrease to 0.2% and 1.6% (1-sigma), assuming the same number of flybys. Finally, performing low-altitude flybys with a pericenter of 2 km, as during the Payload Deployment Phase, the 1-sigma uncertainties in the masses of Didymos primary and secondary can reach the lowest values of 0.01% and 1%, respectively.

However, with the assumed concept of operations and number of flybys, the higher degree gravity of both primary and secondary are not fully observable.

Given the small mass of the Didymos system, optical navigation images proved to be crucial to improve the estimation accuracy of the scientific parameters of interest. The GM of Didymos primary is provided by both Doppler and optical measurements, while the GM of the secondary is mainly given observing the wobble of the primary around the common center of mass due to the mutual orbital motion. Moreover, the optical measurements are essential also to retrieve the secondary orbital motion around the primary, which can be estimated to better than 10 m (1-sigma), and the rotational states of both primary and the secondary, which can be estimated to about 0.1 deg and 0.4 deg (1-sigma), respectively. The libration amplitude, period, and phase of Didymos secondary can be estimated to about 0.03 deg (0.05 m on the equator surface), 9.7 s, and 6.7 deg, respectively (1-sigma).

Different measurement strategies were compared. As a result, it is recommended to use always both Doppler and optical measurements because, even if this measurement strategy does not provide always the best performances for all the estimated parameters, it proved much more reliable and robust, e.g. to constraints in the Sun phase angle, and it allows to better break the scaling symmetry inherent to the optical measurements.

Regarding the experiment geometry, the AIM spacecraft operations shall be designed to optimize the optical measurements coverage of both bodies and maximize the number of pictures collected during the flybys.

Future developments of this work may include an assessment of the observability of the DART impact on Didymos secondary, and in particular of the effects on its orbital and rotational motion, to better constraint the impact performances. Another area of interest is to study methodologies to improve the estimation of higher gravity degrees of the primary and secondary, to better study their internal mass distribution. This would require staying within the sphere of influence of Didymos for longer times, thus a possibility is to exploit satellite-to-satellite range and range-rate measurements between AIM and one or more CubeSats orbiting within the system, and/or the lander deployed on the secondary. Another possibility to be investigated is to exploit periodic or quasi-periodic orbits closer to Didymos, such as terminator orbits or interior retrograde orbits (Dell'Elce et al., 2017)(Lasagni Manghi et al., 2017), that may be used by AIM during the final phase of the mission.

9. Acknowledgements

References

Bills, B.G., Asmar, S.W., Konopliv, A.S., Park, R.S., Raymond, C.A., 2014. Harmonic and statistical analyses of the gravity and topography of Vesta. Icarus 240, 161–173. doi:10.1016/j.icarus.2014.05.033

Cheng, A.F., Atchison, J., Kantsiper, B., Rivkin, A.S., Stickle, A., Reed, C., Galvez, A., Carnelli, I., Michel, P., Ulamec, S., 2015. Asteroid Impact and Deflection Assessment mission. Acta Astronaut. 115, 262–269. doi:10.1016/j.actaastro.2015.05.021

Cheng, A.F., Michel, P., Jutzi, M., Rivkin, A.S., Stickle, A., Barnouin, O., Ernst, C., Atchison, J., Pravec, P., Richardson, D.C., 2016. Asteroid Impact & Deflection Assessment mission: Kinetic impactor. Planet. Space Sci. 121, 27–35. doi:10.1016/j.pss.2015.12.004

Dell'Elce, L., Baresi, N., Naidu, S.P., Benner, L.A.M., Scheeres, D.J., 2017. Numerical investigation of the dynamical environment of 65803 Didymos. Adv. Sp. Res. 59, 1304–1320. doi:10.1016/j.asr.2016.12.018

Evans, S., Taber, W., Drain, T., Smith, J., Wu, H., Guevara, M., Sunseri, R., Evans, J., 2016. Monte: the Next Generation of Mission Design & Navigation Software. 6th International Conference on Astrodynamics Tools and Techniques, Darmstadt, Germany. https://indico.esa.int/indico/event/111/session/30/contribution/177/material/paper/0.pdf

Fang, J., Margot, J.-L., 2012. Near-Earth Binaries and Triples: Origin and Evolution of Spin-Orbital Properties. Astron. J. 143, 24. doi:10.1088/0004-6256/143/1/24

Godard, B., Budnik, F., Munoz, P., Morley, T., 2015. Orbit Determination of Rosetta Around Comet 67P/Churyumov-Gerasimenko. 25th International Symposium on Space Flight Dynamics, Munich, Germany, 2015. doi:10.1017/CBO9781107415324.004

Grieger, B., Kuppers, M., 2016. Determining the mass of Didymos' secondary by visual imaging. Presentation at the EGU General Assembly. Abstract published in Geophysical Research Abstracts, 18, EGU2016-12296. http://meetingorganizer.copernicus.org/EGU2016/EGU2016-12296.pdf

Herfort, Ulrich, and C. Casas. Trajectory Preparation for the Approach of Spacecraft Rosetta to Comet 67P/Churyumov-Gerasimenko. 25th International Symposium on Space Flight Dynamics, Munich, Germany, 2015. http://issfd.org/2015/files/downloads/papers/074_Herfort.pdf

Iess, L., Jacobson, R.A., Ducci, M., Stevenson, D.J., Lunine, J.I., Armstrong, J.W., Asmar, S.W., Racioppa, P., Rappaport, N.J., Tortora, P., 2012. The tides of Titan. Science 337, 457–459. doi:10.1126/science.1219631

Iess, L., Di Benedetto, M., James, N., Mercolino, M., Simone, L., Tortora, P., 2014. Astra: Interdisciplinary study on enhancement of the end-to-end accuracy for spacecraft tracking techniques. Acta Astronaut. 94, 699-707. doi:10.1016/j.actaastro.2013.06.011

Iess, L., Stevenson, D.J., Parisi, M., Hemingway, D., Jacobson, R.A., Lunine, J.I., Nimmo, F., Armstrong, J.W., Asmar, S.W., Ducci, M., Tortora, P., 2014. The gravity field and interior structure of Enceladus. Science 344, 78–80. doi:10.1126/science.1250551

Kato, T., Van Der Ha, J.C., 2012. Precise modelling of solar and thermal accelerations on Rosetta. Acta Astronaut. 72, 165–177. doi:10.1016/j.actaastro.2011.09.009

Konopliv, A.S., Asmar, S.W., Park, R.S., Bills, B.G., Centinello, F., Chamberlin, A.B., Ermakov, A., Gaskell, R.W., Rambaux, N., Raymond, C.A., Russell, C.T., Smith, D.E., Tricarico, P., Zuber, M.T., 2014. The Vesta gravity field, spin pole and rotation period, landmark positions, and ephemeris from the Dawn tracking and optical data. Icarus 240, 103–117. doi:10.1016/j.icarus.2013.09.005

Lasagni Manghi, R., Modenini, D., Zannoni M., Tortora P., 2017. Preliminary Orbital Analysis for a Cubesat Mission to the Didymos Binary Asteroid System, submitted to Advances in Space Research.

Margot, J.-L., Pravec, P., Taylor, P., Carry, B., Jacobson, S., 2015. Asteroid Systems: Binaries, Triples, and Pairs, in: Asteroids IV, 355-374, University of Arizona, Tucson. doi:10.2458/azu_uapress_9780816532131-ch019

Michel, P., Cheng, A., Kuppers, M., Pravec, P., Blum, J., Delbo, M., Green, S.F., Rosenblatt, P., Tsiganis, K., Vincent, J.B., Biele, J., Ciarletti, V., Herique, A., Ulamec, S., Carnelli, I., Galvez, A., Benner, L., Naidu, S.P., Barnouin, O.S., Richardson, D.C., Rivkin, A., Scheirich, P., Moskovitz, N., Thirouin, A., Schwartz, S.R., Campo Bagatin, A., Yu, Y., 2016. Science case for the Asteroid Impact Mission (AIM): A component of the Asteroid Impact & Deflection Assessment (AIDA) mission. Adv. Sp. Res. 57, 2529–2547. doi:10.1016/j.asr.2016.03.031

Modenini, D., Tortora, P., 2014. Pioneer 10 and 11 orbit determination analysis shows no discrepancy with Newton-Einstein laws of gravity. Phys. Rev. D 90, 022004. doi:10.1103/PhysRevD.90.022004

Moyer, T. D., 1971. Mathematical formulation of the Double-Precision Orbit Determination Program (DPODP). Technical Report 32-1527, Jet Propulsion Laboratory, Pasadena (CA).

Moyer, T. D., 2000. Formulation for Observed and Computed Values of Deep Space Network Data Types for Navigation. Wiley, Hoboken (NJ). doi:10.1002/0471728470

Osip, D.J., Rivkin, A.S., Pravec, P., Moskovitz, N., Thirouin, A., Scheirich, P., Oszkiewicz, D.A., Richardson, D.C., Polishook, D., Ryan, W., Thomas, C., Busch, M.W., Cheng, A.F., Michel, P., 2016. The Observing Working Group for the Asteroid Impact & Deflection Assessment (AIDA) Mission. AAS/Division for Planetary Sciences Meeting Abstracts, 48. http://adsabs.harvard.edu/abs/2016DPS....4812322O

Pardo de Santayana, R., Lauer, M., 2015. Optical Measurements for Rosetta Navigation Near the Comet. 25th International Symposium on Space Flight Dynamics, Munich, Germany. http://issfd.org/2015/files/downloads/papers/062_Pardo.pdf

Pravec, P., Scheirich, P., Kušnirák, P., Šarounová, L., Mottola, S., Hahn, G., Brown, P., Esquerdo, G., Kaiser, N., Krzeminski, Z., Pray, D.P., Warner, B.D., Harris, A.W., Nolan, M.C., Howell, E.S., Benner, L.A.M., Margot, J.L., Galád, A., Holliday, W., Hicks, M.D., Krugly, Y.N., Tholen, D., Whiteley, R., Marchis, F., DeGraff, D.R., Grauer, A., Larson, S., Velichko, F.P., Cooney, W.R., Stephens, R., Zhu, J., Kirsch, K., Dyvig, R., Snyder, L., Reddy, V., Moore, S., Gajdoš, Š., Világi, J., Masi, G., Higgins, D., Funkhouser, G., Knight, B., Slivan, S., Behrend, R., Grenon, M., Burki, G., Roy, R., Demeautis, C., Matter, D., Waelchli, N., Revaz, Y., Klotz, A., Rieugné, M., Thierry, P., Cotrez, V., Brunetto, L., Kober, G., 2006. Photometric survey of binary near-Earth asteroids. Icarus 181, 63–93. doi:10.1016/j.icarus.2005.10.014

Richardson, D.C., Barnouin, O.S., Benner, L.A.M., Bottke Jr., W.F., Campo Bagatín, A., Cheng, A.F., Hirabayashi, M., Maurel, C., McMahon, J.W., Michel, P., Murdoch, N., Naidu, S.P., Pravec, P., Rivkin, A.S., Scheeres, D.J., Scheirich, P., Tsiganis, K., Zhang, Y., Group, the A.D. and P.P. of D.W., 2016. Dynamical and physical properties of 65803 Didymos. 47th Lunar and Planetary Science Conference, 1501. doi:10.1038/ngeo2474.

Scheirich, P., Pravec, P., 2009. Modeling of lightcurves of binary asteroids. Icarus 200, 531–547. doi:10.1016/j.icarus.2008.12.001

Tortora, P., Zannoni, M., Hemingway, D., Nimmo, F., Jacobson, R.A., Iess, L., Parisi, M., 2016. Rhea gravity field and interior modeling from Cassini data analysis. Icarus 264, 264–273. doi:10.1016/j.icarus.2015.09.022

Tsoulis, D., Jamet, O., Verdun, J., Gonindard, N., 2009. Recursive algorithms for the computation of the potential harmonic coefficients of a constant density polyhedron. J. Geod. 83, 925–942. doi:10.1007/s00190-009-0310-9

Werner, R.A., 1997. Spherical harmonic coefficients for the potential of a constant-density polyhedron. Comput. Geosci. 23, 1071–1077. doi:10.1016/S0098-3004(97)00110-6

Werner, R.A., Scheeres, D.J., 1997. Exterior gravitation of a polyhedron derived and compared with harmonic and mascon gravitation representations of asteroid 4769 Castalia. Celest. Mech. Dyn. Astron. 65, 313–344. doi:10.1007/BF00053511

Wieczorek, M.A., Phillips, R.J., 1998. Potential anomalies on a sphere: Applications to the thickness of the lunar crust. J. Geophys. Res. 103, 1715. doi:10.1029/97JE03136

1
2
3
4
5
6
7
8
9
10
11
12
13
14
15
16
17
18
19
20
21
22
23
24
25
26
27
28
29
30
31
32
33
34
35
36
37
38
39
40
41
42
43
44
45
46
47
48
49
50
51
52
53
54
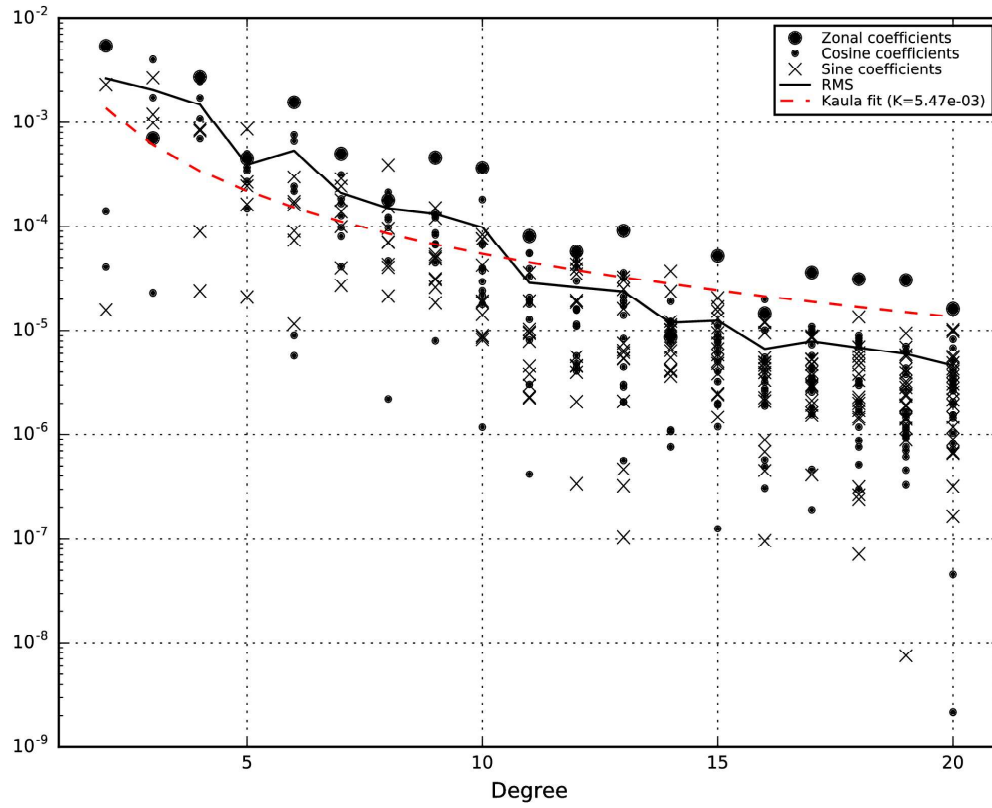55
56
57
58
59
60
61
62
63
64
65

Figures

Figure 1 Gravitational model of Didymos primary: absolute value of spherical harmonics normalized coefficients up to degree 20; RMS of coefficients for each degree; fit of degree RMS using Kaula's rule (best fit K: 5.47x10^-3).
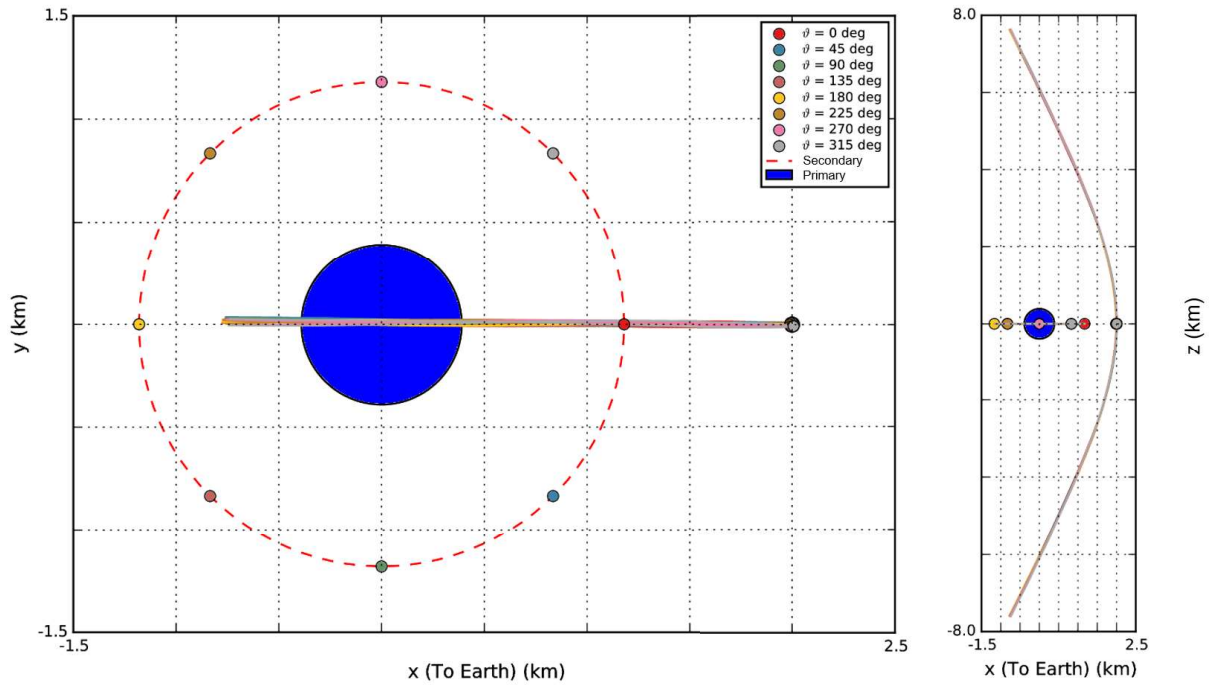
Figure 2 Example of spacecraft trajectories during 8 radio science flybys, defined by the following parameters: rp = 2 km, i = 90 deg, Ωp = 0 deg, ωp = 0 deg. For clarity, the spacecraft trajectory is represented only during a time interval of 8 h around the flyby closest approach. The trajectory of the spacecraft during different arcs is represented using different colors, but no difference are visible, because the same initial conditions are used. The position of the spacecraft and Didymos secondary at the pericenter epoch is identified by a colored circle. Each arc is identified by a different color, as described in the legend. The adopted reference frame is: +z Didymos pole; +x along Earth direction, perpendicular to z; center in the Didymos system center of mass.
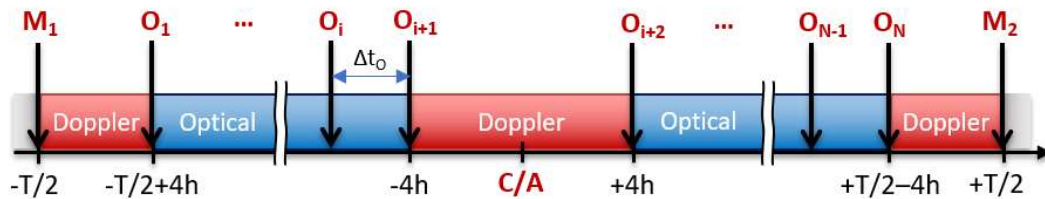
Figure 3 Timeline of an arc of duration T (nominal: 72 h) dedicated to radio science investigations. The arc is symmetrical around the flyby closest approach to the Didymos system (C/A). The arc starts and ends with the orbital maneuvers M_1 and M_2, respectively. Doppler coverage consists of three 8-h tracking passes around the maneuvers and the flyby C/A, so that only 4 h of data during the first and last tracking passes can be used in the radio science estimation. Between tracking periods, optical observables O_i are acquired, with a sampling time of Δt_O (nominal: 2 h).
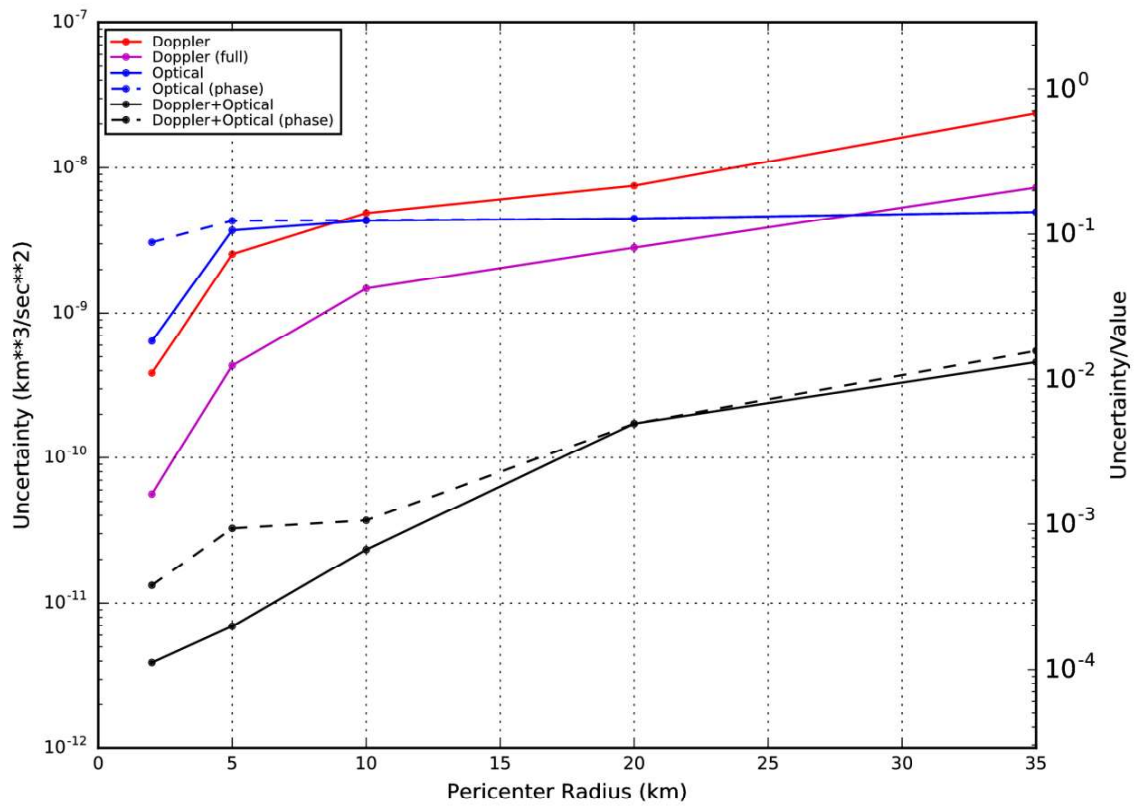
Figure 4 Measurement strategies comparison: Didymos primary GM formal 1-sigma uncertainty vs pericenter distance. For each pericenter distance the minimum uncertainty over all the possible orbital planes is displayed.
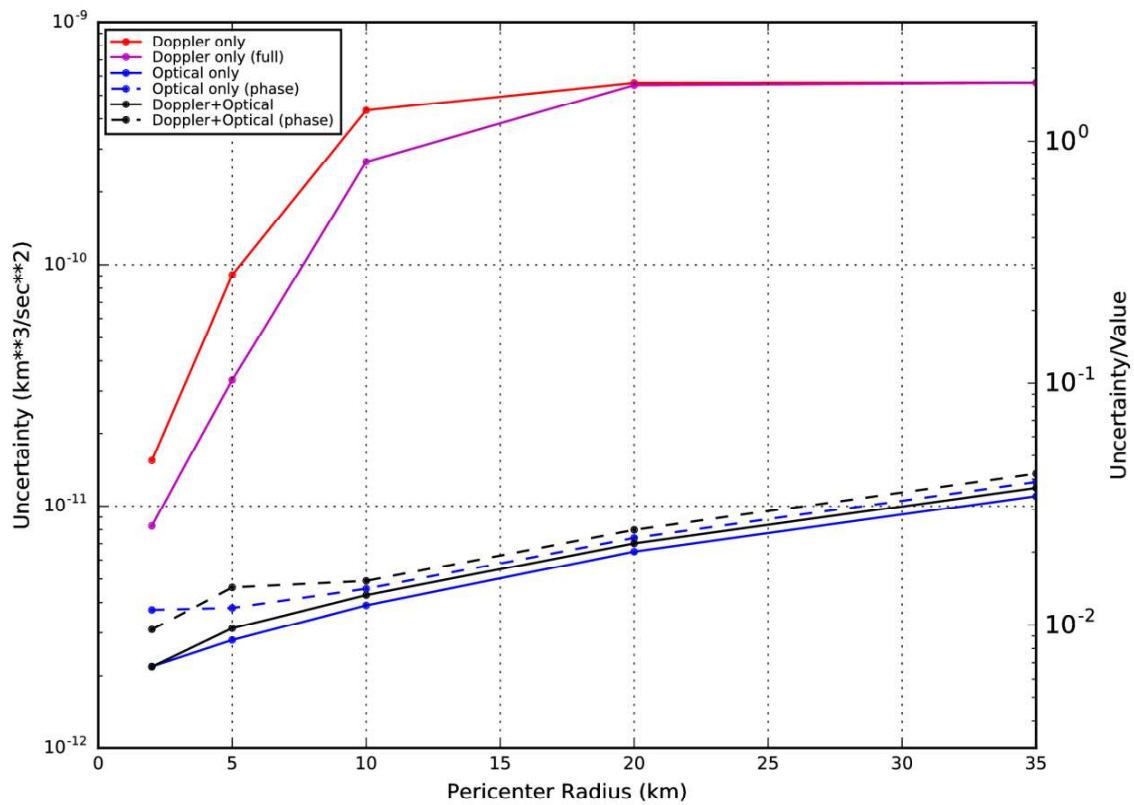
Figure 5 Measurement strategies comparison: Didymos secondary GM formal 1-sigma uncertainty vs pericenter distance. For each pericenter distance the minimum uncertainty over all the possible orbital planes is displayed.

Tables

Table 1 Reference timeline of the AIM mission adopted in this study.

Event	Date	Duration	Comments
Launch	17/10/2020 06/11/2020	-	Several options possible.
Arrival to Didymos system	24/04/2022	-	At latest.
Early Characterization Phase (ECP)	22/05/2022	~4 weeks	AIM-Didymos distances: about 35 km.
Detailed Characterization Phase Period 1 (DCP1)	19/06/2022	~4 weeks	AIM-Didymos distance reduced to about 10 km.
Payload Deployment Phase (PDP)	17/07/2022	~4 weeks	Possibility to perform a limited number of low altitude flybys to better characterize Didymos system dynamical parameters before CubeSats and Lander deployments.
PDP: CubeSats deployment	31/07/2022 00:00:00 TDB	-	Assumed CubeSats deployment date for this study.
PDP: Lander deployment	07/08/2022 00:00:00 TDB	-	Assumed Lander deployment date for this study.
Detailed Characterization Phase Period 2 (DCP2)	14/08/2022	~4 weeks	Similar to DCP1.
Impact Phase (IP)	11/09/2022	~3 weeks	AIM at a safe distance from Didymos (about 100 km).
IP: DART impact	21/09/2022 00:00:00 TDB	-	Assumed impact date for this study.
Detailed Characterization Phase Period 3 (DCP3)	02/10/2022	~3 months	Gradually return to orbits similar to DCP1 and DCP2.
Disposal Phase	21/12/2022	TBD	
End of Life (EoL)	22/12/2022	-	AIM disposal.

Table 2 Parameters which uniquely defines the AIM trajectory with respect to Didymos during a Radio Science experiment. For each parameter the allowable interval adopted in this study is provided. The adopted quasi-inertial reference frame is: +z Didymos pole; +x along Earth direction, perpendicular to z; center in the Didymos system center of mass.

Parameter	Symbol	Values	Comments
Pericenter radius	r_p	2.0 – 35 km	Different values were studied.
Pericenter velocity	v_p	1.4 x v_e = 26.5 – 6.5 cm/s	v_e: escape velocity at pericenter. Higher for smaller pericenter radii and vice versa.
Inclination	i	0–180 deg	Different values covering all possible orbital planes were studied.
Longitude of pericenter	Ω_p	0-360 deg	Different values covering all possible orbital planes were studied.
Argument of pericenter	ω_p	0-360 deg	Different values covering all possible orbital planes were studied.
Didymos secondary true anomaly at pericenter epoch	ϑ_p	0–360 deg	The parameter takes into account the synchronization between the spacecraft and Didymos secondary.

Table 3 Order of magnitude of the main accelerations acting on AIM. The nominal values of the AIM and Didymos parameters used to compute the accelerations were: primary gravitational parameter GM_1 = 3.4903x10^{-8} km^3/s^2; secondary gravitational parameter GM_2 = 3.23x10^{-10} km^3/s^2; primary radius R_1 = 390 m; secondary radius R_2 = 82 m; primary J_2 = 0.012; secondary J_2' = 0.077; AIM area A = 10 m^2; AIM mass M = 600 kg; Solar flux at Earth ϕ_s = 1380 W/m^2; AIM surface absorption coefficient α = 0.8; AIM surface temperature normalized difference $\Delta T/T_0$ = 0.25; primary average effective temperature T_1 = 250 K; primary bond albedo a_1 = 0.07.

Contribution	Formula	Acceleration (m/s^2)				
		r = 1 km	r = 5 km	r = 10 km	r = 20 km	r = 35 km
Primary monopole	GM_1/r^2	3.5 x10^{-5}	1.4 x10^{-6}	3.5 x10^{-7}	8.8 x10^{-8}	2.9 x10^{-8}
Secondary monopole	GM_2/r^2	3.2 x10^{-7}	1.3 x10^{-8}	3.2 x10^{-9}	8.0 x10^{-10}	2.6 x10^{-10}
Primary quadrupole	$3\left(\dfrac{GM_1}{r^2}\right)\left(\dfrac{R_1}{r}\right)^2 J_2$	8.7 x10^{-8}	1.4 x10^{-10}	8.7 x10^{-12}	5.5 x10^{-13}	5.8 x10^{-14}
Secondary quadrupole	$3\left(\dfrac{GM_2}{r^2}\right)\left(\dfrac{R_2}{r}\right)^2 J_2'$	2.2 x10^{-12}	3.6 x10^{-15}	2.2 x10^{-16}	1.4 x10^{-17}	1.5 x10^{-15}
Sun gravity perturbation	$2(GM_s/r_s^3)r$	1.3 x10^{-11}	6.6 x10^{-11}	1.3 x10^{-10}	2.7 x10^{-10}	4.6 x10^{-10}
Solar Radiation Pressure	$\dfrac{A}{M}\dfrac{\Phi_s}{c}$	7.7 x10^{-8}				

Thermal Recoil Pressure	$\dfrac{4}{9}\dfrac{A}{M}\dfrac{\Phi_s}{c}\dfrac{\alpha\Delta T}{T_0}$	6.8 x10^{-9}				
Primary thermal re-emission	$\dfrac{A}{M}\dfrac{\sigma T_1^4}{c}\left(\dfrac{R_1}{r}\right)^2$	1.9 x10^{-9}	7.5 x10^{-11}	1.9 x10^{-11}	4.7 x10^{-12}	1.5 x10^{-12}
Primary albedo	$\dfrac{A}{M}\dfrac{\Phi_s}{c}a_1\left(\dfrac{R_1}{r}\right)^2$	8.2 x10^{-10}	3.3 x10^{-11}	8.2 x10^{-12}	2.0 x10^{-12}	6.7 x10^{-13}

Table 4 Shape model of AIM assumed for this study.

Component	Area (m^2)	Specular Reflectivity	Diffusive Reflectivity	Comments
HGA	2.5	0.0	0.327	Fixed HGA. Diameter: 1.8 m.
Bus top/bottom	3.6	0.0735	0.252	One two-sided flat plate. Dimensions: 2.0x1.8 m.
Bus sides	3.7	0.0735	0.252	One two-sided flat plate. Dimensions: 2.1x1.8 m.
Bus front/rear	4.2	0.0735	0.252	One two-sided flat plate. No shadowing with HGA. Dimensions: 2.1x2.0 m.
Solar Arrays	5.6	0.038	0.052	Fixed solar arrays. One two-sided flat plate with total area of the two arrays.

Table 5 Rotational model of Didymos primary and secondary. The base reference frame is Earth Mean Orbit at J2000 (EMO2000). The reference epoch is April 24th, 2022.

Parameter		Value	Comments
Didymos Primary	α_0	310 deg	Pole solution II of (Scheirich and Pravec, 2009).
	α_1	0.0 deg/century	Not measured at present. Assumed zero.
	δ_0	-84 deg	Pole solution II of (Scheirich and Pravec, 2009).
	δ_1	0.0 deg/century	Not measured at present. Assumed zero.
	w_0	0.0 deg	This term defines the prime meridian. Assumed zero.
	w_1	159.29 deg/h	From rotation period.
Didymos Secondary	α_0	-49.97 deg	Fitted to a dynamical synchronous model.
	α_1	-25.58 deg/century	Fitted to a dynamical synchronous model.
	δ_0	-84.01 deg	Fitted to a dynamical synchronous model.

δ_1	6.76 deg/century	Fitted to a dynamical synchronous model.	
w_0	190.14 deg	Fitted to a dynamical synchronous model.	
w_1	30.37 deg/h	Fitted to a dynamical synchronous model.	
w_a	1.0 deg	Consistent with (Richardson et al., 2016).	
ω	30.20 deg/h	Assumed equal to the average orbital period.	
φ	6.71 deg	Fitted to a dynamical synchronous model.	

Table 6 Gravitational model of Didymos primary and Secondary: spherical harmonics normalized coefficients of degree 2, rounded to 2 decimal places, for clarity. For Didymos primary, a full 20-degree model was adopted in the simulations. The reference radii for the primary and the secondary are 0.43 km and 0.103 km, respectively. The adopted GMs for the primary and the secondary are 3.4903×10^{-8} km^3/s^2 and 3.23×10^{-10} km^3/s^2, respectively.

l	m	Didymos primary		Didymos secondary	
		Clm	Slm	Clm	Slm
2	0	-5.44e-03	0.0	-7.67e-02	0.0
2	1	4.09e-05	-1.58e-05	0.0	0.0
2	2	-1.41e-04	2.31e-03	2.06e-02	0.0

Table 7 Filter setup summary.

Parameter	Type	A priori uncertainty (1-sigma)	Comments
Spacecraft state	Position	local	100 km	Spacecraft state with respect to Didymos system center of mass.
	Velocity	local	1.0 m/s	Virtually unconstrained. Big enough to account for the maneuver errors at the beginning of the arc.
Didymos system state	Position	global	100 km	Conservatively assumed equal to three times Rosetta's 1-sigma formal uncertainty of the heliocentric state of comet 67P/Churyumov-Gerasimenko (Godard et al., 2015).
	Velocity	global	1.0 cm/s	
Didymos secondary state	Position	local	0.4 km	10 times the measured uncertainty in semi-major axis. Virtually unconstrained. The corresponding a priori uncertainty in Didymos primary's position is about 20 m.
	Velocity	local	30 mm/s	From the measured uncertainty in semi-major axis, scaled by a factor 10. It corresponds to 20% of the a priori orbital velocity. The corresponding a priori uncertainty in Didymos primary's velocity is about 3 mm/s.

Didymos primary gravity	GM	global	3.57×10^{-8} km^3/s^2	From the measured uncertainty in the total mass of Didymos system, scaled by a factor of 10. Virtually unconstrained.
	C_{20}	global	5.44×10^{-2}	Normalized coefficients. Base uncertainty equal to value, then multiplied by a factor of 10. Virtually unconstrained.
	C_{22}	global	1.41×10^{-3}	
	S_{22}	global	2.31×10^{-2}	
	C_{21}	global	1.62×10^{-3}	Normalized coefficient. Computed assuming a maximum misalignment of 10 deg between the body-fixed frame and the principal inertia axes. Virtually unconstrained.
	S_{21}	global	1.67×10^{-3}	
Didymos secondary gravity	GM	global	5.65×10^{-10} km^3/s^2	From the measured uncertainties in the total mass of Didymos system and the diameter ratio between primary and secondary, scaled by a factor of 10. Virtually unconstrained.
	C_{20}	global	3.43×10^{-1}	Normalized coefficients. Base uncertainty equal to value, then multiplied by a factor of 10. Virtually unconstrained.
	C_{22}	global	3.19×10^{-1}	
	C_{21}	global	1.59×10^{-2}	Normalized coefficients. Computed assuming a maximum misalignment of 10 deg between the body-fixed frame and the principal inertia axes. Virtually unconstrained.
	S_{21}	global	4.80×10^{-3}	
	S_{22}	global	1.11×10^{-2}	
Didymos primary frame	α_0	global	50 deg	From the measured uncertainties, scaled by a factor of 5. Virtually unconstrained.
	δ_0	global	10 deg	
	α_1	global	3.5×10^{-3} deg/h	Equal to w_1 uncertainty divided by 10. Typically much smaller than the uncertainty in the rotational period.
	δ_1	global	3.5×10^{-3} deg/h	
	w_1	global	3.5×10^{-2} deg/h	From the measured uncertainty in the orbital period, scaled by a factor of 5.
Didymos secondary frame	α_0	global	50 deg	Same as Didymos primary. Virtually unconstrained.
	δ_0	global	10 deg	
	α_1	global	7.6×10^{-3} deg/h	Equal to w_1 uncertainty divided by 10. Typically much smaller than the uncertainty in the rotational period.
	δ_1	global	7.6×10^{-3} deg/h	
	w_1	global	7.6×10^{-2} deg/h	From the orbital period uncertainty, scaled by a factor of 5.
	w_a	global	50 deg	Virtually unconstrained.
	ω	global	7.6×10^{-2} deg/h	Equal to w_1 uncertainty.
	φ	global	50 deg	Virtually unconstrained.

SRP	Scale factor	local	1.0	Uncertainty: 100% of the acceleration.
TRP	3 accel.	local	7.2×10^{-12} km^3/s^2	100% of the expected value.
Pointing error per picture	3 rotations	local	10 mdeg	From Rosetta.
Didymos primary landmarks position	Scale factor	global	0.1	10% size scale, common to all landmarks.
	Radius	global	39 m	10% of the radius in the three directions, for each landmark.
	Lat., Long.	global	5.7 deg	
Didymos secondary landmarks position	Scale factor	global	0.1	10% size scale, common to all landmarks.
	Radius	global	8.2 m	10% of the radius in the three directions, for each landmark.
	Lat., Long.	global	5.7 deg	

Table 8 Summary of best formal 1-sigma uncertainties achievable by the AIM Radio Science Experiment, using both Doppler and optical measurements. For clarity, only the main parameters of interest are displayed. Three mission phases are compared: Early Characterization Phase (ECP), with a pericenter distance of 35 km; Detailed Characterization Phase 1 (DCP1), with a pericenter distance of 10 km; Payload Deployment Phase (PDP), with a pericenter distance of 2 km. Between brackets the relative uncertainty with respect to a reference value is displayed.

Parameter	Unit	ECP (r = 35 km)	DCP1 (r = 10 km)	PDP (r = 2 km)	Comments
Spacecraft Radial Position	m	320 (0.9%)	7.7 (0.08%)	0.54 (0.03%)	Approximate radial uncertainty at pericenter epoch with respect to Didymos primary (average over all the arcs). Reference value: pericenter radius.
Didymos Secondary Radial Position	m	11 (0.9%)	1.1 (0.09%)	0.55 (0.05%)	Approximate radial uncertainty at pericenter epoch with respect to Didymos primary (average over all the arcs). Reference value: nominal orbital radius (1.18 km).
Didymos Secondary Orbital Period	min	14 (2%)	1.8 (0.3%)	0.64 (0.09%)	Uncertainty at pericenter epoch. Reference value: nominal orbital period (11.9 h).
Didymos Primary GM	km^3/s^2	7.0×10^{-10} (2%)	5.9×10^{-11} (0.2%)	1.8×10^{-11} (0.05%)	Reference value: body GM (primary: 3.4903×10^{-8} km^3/s^2; secondary: 3.23×10^{-10} km^3/s^2).
Didymos Secondary GM	km^3/s^2	1.4×10^{-11} (4%)	5.1×10^{-12} (1.6%)	3.2×10^{-12} (1%)	
Didymos Primary Pole	deg	0.25	0.07	0.13	RSS of RA and DEC uncertainties. Didymos secondary frame not estimated

Parameter	Unit				Notes
Didymos Secondary Pole	deg	N/A	0.37	0.42	during ECP because the distance from Didymos was considered too large to observe landmarks.
Didymos Secondary Libration Amplitude	deg	N/A	0.03	0.05	Not estimated during ECP because the distance from Didymos is considered too large to observe landmarks. Reference value for libration amplitude: nominal amplitude (1 deg).
Didymos Secondary Libration Period	s	N/A	9.7 (0.02%)	13 (0.03%)	Reference value for libration period: nominal orbital period (11.9 h).
Didymos Secondary Libration Phase	deg	N/A	6.7	8.3	
Didymos Primary Landmarks Position	m	4.0 (1%)	3.5 (0.9%)	4.0 (1%)	RSS of 3-D position uncertainty. Approximate average values over all landmarks. Reference values: average radii (primary: 390 m; secondary: 81.9 m).
Didymos Secondary Landmarks Position	m	N/A	1.3 (2%)	1.2 (1%)	Didymos secondary landmarks not estimated during ECP because the distance from Didymos is considered too large to observe landmarks.

Table 9 Summary of formal 1-sigma uncertainties achievable using both Doppler and optical measurements, but processing only pictures of either Didymos primary or secondary. The same cases as in Table 8 are displayed. For clarity, only a subset of the estimated parameters is shown. The ratio between the uncertainties shown Table 8 and those obtained here is also displayed between brackets.

Parameter	Unit	Didymos Primary Only			Didymos Secondary Only		
		ECP (r = 35 km)	DCP1 (r = 10 km)	PDP (r = 2 km)	ECP (r = 35 km)	DCP1 (r = 10 km)	PDP (r = 2 km)
Spacecraft Radial Position	m	510 (1.6)	9.4 (1.2)	0.95 (1.8)	790 (2.5)	14 (1.8)	0.90 (1.7)
Didymos Secondary Radial Position	m	160 (14)	85 (79)	60 (110)	210 (2.0)	3.5 (3.2)	0.86 (1.6)
Didymos Primary GM	km³/s²	1.0×10^{-9} (1.5)	6.9×10^{-11} (1.2)	2.9×10^{-11} (1.6)	1.9×10^{-9} (2.7)	1.8×10^{-10} (3.0)	3.2×10^{-11} (1.7)
Didymos Secondary GM	km³/s²	1.6×10^{-11} (1.2)	5.9×10^{-12} (1.2)	4.3×10^{-12} (1.3)	3.1×10^{-10} (23)	1.1×10^{-10} (22)	4.9×10^{-12} (1.5)

Table 10 Summary of the formal 1-sigma uncertainties achievable in the single-arc estimations. Each arc is characterized by a different true anomaly ϑ_p of Didymos secondary at the flyby pericenter time. The same cases as in Table 8 are displayed. For clarity, only the GM of Didymos primary and secondary is shown. The ratio between the uncertainties shown Table 8 and those obtained here is also displayed between brackets.

Arc Number	Arc ϑ_p (deg)	Didymos Primary GM (km^3/s^2)			Didymos Secondary GM (km^3/s^2)		
		ECP (r = 35 km)	DCP1 (r = 10 km)	PDP (r = 2 km)	ECP (r = 35 km)	DCP1 (r = 10 km)	PDP (r = 2 km)
1	0	1.9×10^{-9} (2.7)	4.6×10^{-10} (7.9)	8.2×10^{-11} (4.5)	3.9×10^{-11} (2.8)	1.5×10^{-11} (2.9)	9.8×10^{-12} (3.0)
2	45	1.9×10^{-9} (2.7)	4.3×10^{-10} (7.4)	8.0×10^{-11} (4.3)	3.9×10^{-11} (2.8)	1.5×10^{-11} (2.9)	1.1×10^{-11} (3.5)
3	90	1.9×10^{-9} (2.8)	4.2×10^{-10} (7.2)	7.4×10^{-11} (4.0)	3.9×10^{-11} (2.8)	1.5×10^{-11} (2.9)	1.0×10^{-11} (3.1)
4	135	2.0×10^{-9} (2.9)	4.2×10^{-10} (7.2)	7.1×10^{-11} (3.9)	3.9×10^{-11} (2.9)	1.5×10^{-11} (2.9)	1.1×10^{-11} (3.4)
5	180	2.1×10^{-9} (2.9)	4.1×10^{-10} (7.0)	7.1×10^{-11} (3.9)	3.9×10^{-11} (2.8)	1.4×10^{-11} (2.8)	1.2×10^{-11} (3.6)
6	225	2.1×10^{-9} (3.0)	3.9×10^{-10} (6.7)	7.2×10^{-11} (3.9)	3.8×10^{-11} (2.8)	1.4×10^{-11} (2.8)	1.3×10^{-11} (3.7)
7	270	2.1×10^{-9} (3.1)	3.9×10^{-10} (6.6)	7.2×10^{-11} (3.9)	3.9×10^{-11} (2.8)	1.5×10^{-11} (2.9)	8.8×10^{-12} (2.7)
8	315	2.2×10^{-9} (3.1)	3.8×10^{-10} (6.4)	7.5×10^{-11} (4.1)	3.9×10^{-11} (2.8)	1.5×10^{-11} (2.9)	8.6×10^{-12} (2.7)